Realignment Technique on a Low-Complexity Algorithm for Orbit Prediction in the Circular Restricted Three-Body Problem

Vikas A. Patel*, Brian Baker-McEvilly†, David Canales‡, and Sirani M. Perera§
Embry-Riddle Aeronautical University, Daytona Beach, Florida, 32114

Exponential traffic growth in the Cislunar realm emphasizes the need for precise trajectory prediction within the circular restricted three-body problem. Traditional numerical trajectory prediction methods in situations with complex dynamics are often computationally expensive. Thus, low-complexity algorithms are needed for trajectory prediction. This study builds upon previous work on a low-complexity algorithm and explores its capabilities for extrapolating orbital trajectories. The extended LCA method is demonstrated on various Cislunar trajectories, showcasing its effectiveness in minimizing errors while predicting future trajectories. In cases where limited measurements are known of an object, the eLCA provides relatively successful trajectory prediction with fast computation.

I. Introduction

In recent years, the Cislunar region has garnered significant attention from government and commercial space entities due to its potential for scientific discovery and strategic value. This region is foreseen to become increasingly congested with a multitude of missions planned for the near future [1]. Lunar programs, such as Artemis [2], Luna [3], and Chang'E [4], all aim to establish a constant human presence on the lunar surface. Additionally, the Gateway program aims to establish a long-term orbital station about the Moon in a near-rectilinear halo orbit (NRHO), further exemplifying the growing interest in establishing a sustained presence in this region [5, 6]. Historical debris analysis indicates that the increase in missions will lead to a corresponding debris increase, necessitating sophisticated tracking and management strategies [7–9]. Also, there is increased interest in tracking other satellites for both defense and collision avoidance purposes [10–12]. Thus, there is a need for comprehensive space domain awareness (SDA) in the Cislunar region, which requires the tracking and monitoring of objects, both operational and debris. However, sufficient computational resources may not always be available to track these objects using traditional methods, such as aboard a spacecraft or on the Lunar surface. Given this potential for computationally stringent scenarios where orbit propagation and prediction is needed in Cislunar space, it is crucial to develop more accessible and efficient methods. These tools must operate at lower complexities compared to expensive numerical techniques in order to fill the need for low cost trajectory prediction algorithms. By doing so, spacecraft can ensure that they have the necessary capabilities to effectively navigate and anticipate orbital movements in a cost-effective manner.

Traditionally, tracking the state of space objects under the gravitational influence of many bodies involves integrating position and velocity using established dynamic equations of motion. Numerical integration techniques commonly employed include the Runge-Kutta, Gauss-Legendre, Dormand-Prince, Chebyshev-Picard [13], Gragg-Bulirsch-Stoer [14], Adams–Bashforth, or Adams–Moulton [15] methods. While these techniques achieve high accuracy, they do so at the cost of significant computational resources through iterative processes, which may be prohibitive to systems with limited computational resources,i.e., onboard a spacecraft. Previously, the authors have developed a low-complexity algorithm (LCA) for orbit prediction in the CR3BP [16]. The LCA uses polynomial interpolation between known boundary conditions to build a piece-wise continuous function that predicts trajectories. To operate, the LCA requires knowledge of position, velocity, and acceleration at distinct times. It is a computationally efficient method with an arithmetic complexity of $O(n^2)$, as opposed to the brute-force calculation having the complexity of $O(n^3)$. This is achieved through a sparse matrix decomposition based on the coefficient matrix of a system of equations formulated by the polynomial and known boundary conditions. This method has demonstrated its capability to produce relatively accurate results within the bounds of the circular restricted three-body problem (CR3BP) dynamics, offering a significant

---

*Undergraduate Student, Aerospace Engineering Department, patelv27@my.erau.edu
†Ph.D. Student, Aerospace Engineering Department, bakermcb@my.erau.edu
‡Assistant Professor, Aerospace Engineering Department, canaled4@erau.edu
§Associate Professor, Mathematics Department, pereras2@erau.edu

reduction in computation time compared to traditional numerical methods [16]. Previously, the LCA is only analyzed on its accuracy to interpolate between boundary conditions.

This investigation now focuses on the accuracy of the LCA to predict trajectories outside the known boundary conditions as well as developing a technique to lower prediction error when using the LCA, referred to as the extended LCA (eLCA). The eLCA technique incorporates pseudo-measurements that lay outside of known boundary conditions, along with corrected dynamics at that point, that are then used to produce a new arc, estimating the trajectory between the final boundary condition and the psuedo-measurement. This correction technique ensures that the LCA may adapt predictions to evolving trajectories in the Cislunar region, providing more accurate trajectories. Thus, the primary objectives of this investigation are: a) formulate the eLCA technique, b) investigate the limitations and implications of the eLCA, and c) carry out a comparison between the prediction capabilities of LCA, a traditional numerical technique, and the eLCA for orbits in Cislunar space.

The paper is structured as follows. Section II discusses the dynamics of the CR3BP used for modeling and simulations. Subsequently, Section III explains the theory of the LCA and the techniques utilized in the eLCA to achieve the desired results. Section IV details the results of the modelling and simulation of the eLCA, comparing it to the LCA and a numerical method for various Cislunar orbits. Lastly, Section V summarizes the findings of this investigation and outlines opportunities for future efforts.

II. Dynamical Model

The CR3BP is often employed to model the gravitational influence of the Earth and Moon in Cislunar space [17]. The model consists of a large primary body (Earth), a smaller primary body (the Moon), and a third body of negligible mass representing the spacecraft (s/c). The barycenter of the Earth-Moon system acts as the origin of the rotating frame and is defined by the center of mass of the two primaries. It is assumed that the primaries move in circular orbits about the common barycenter. The CR3BP rotating frame is defined as follows: the $\hat{x}$-axis lays the centers of the Earth, the barycenter, and the Moon, the $\hat{z}$-axis points out of the Earth-Moon orbital plane, and the $\hat{y}$-axis completes the right-handed coordinate system. Furthermore, the CR3BP characteristic quantities non-dimensionalize the system: characteristic length is defined as the distance between the two primaries, characteristic time is the period of the Earth-Moon system, and characteristic mass is the total mass of the Earth and Moon. The mass parameter of the CR3BP system defines the location of the barycenter and is given by: $\mu = \frac{m_M}{m_E + m_M}$, where the m_E and m_M are the mass of the Earth and Moon, respectively. The position $\underline{r} = [x, y, z]^{\mathrm{T}} \in \mathbb{R}^3$ and velocity $\dot{\underline{r}} = [\dot{x}, \dot{y}, \dot{z}]^{\mathrm{T}} \in \mathbb{R}^3$ of the spacecraft in the Earth-Moon CR3BP are governed by the following equations of motion:

$$\ddot{x} - 2\dot{y} = \frac{\partial U^*}{\partial x}; \ \ddot{y} + 2\dot{x} = \frac{\partial U^*}{\partial y}; \ \ddot{z} = \frac{\partial U^*}{\partial z} \tag{1}$$

such that U^* is the pseudo-potential function of the system:

$$U^* = \frac{1-\mu}{||\underline{r}_{E-s/c}||} + \frac{\mu}{||\underline{r}_{M-s/c}||} + \frac{1}{2}(x^2 + y^2) \tag{2}$$

where double bars denote magnitudes and $\underline{r}_{E-s/c}$ and $\underline{r}_{M-s/c}$ are the relative position vectors of the Earth and Moon to the spacecraft, respectively. According to [18, 19], the existence of a solution to the governing differential equations, Eq. (1) gives the equilibrium points known as Lagrange points, i.e., L_1 - L_5. These unique locations within the CR3BP are where gravitational and rotational forces find balance, enabling the spacecraft to maintain equilibrium relative to the Earth and the Moon in the rotating frame. A schematic of the CR3BP is provided in Figure 1. Finally, a constant of integration exists within the CR3BP derivation, known as the Jacobi Constant (JC). The JC is calculated via:

$$JC = 2U^* - (\dot{x}^2 + \dot{y}^2 + \dot{z}^2). \tag{3}$$

where the former term ($2U^*$) describes the spacecraft's potential energy, and ($\dot{x}^2 + \dot{y}^2 + \dot{z}^2$) its kinetic energy.

III. Low-complexity trajectory prediction

A. Theory of the LCA

Predicting trajectories in the chaotic regime of the circular restricted three-body problem often entails the use of numerical methods [20]. These numerical methods are iterative and can produce approximated solutions at the

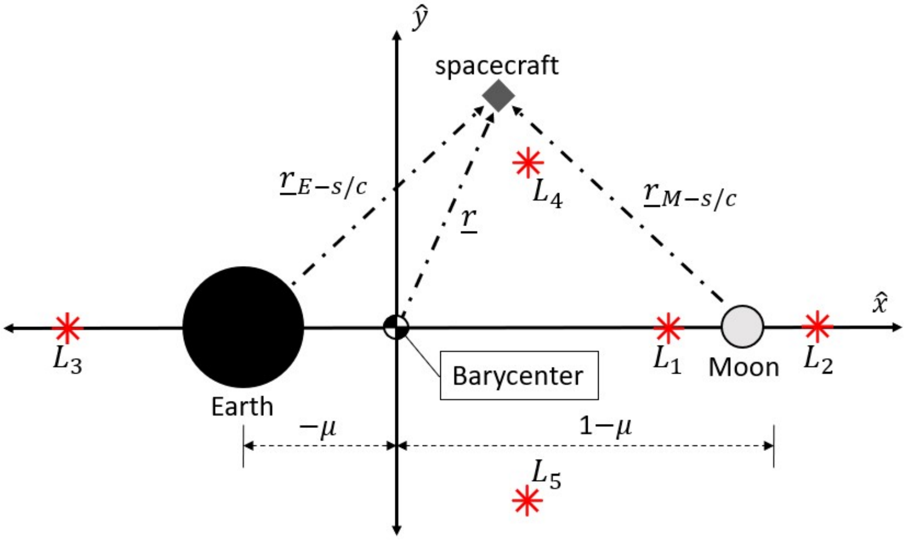

Fig. 1 CR3BP in the Earth-Moon rotating frame.

cost of higher computation. Due to such reasons, these methods may not always be suitable for on-board processes. Alternatively, one could utilize the polynomial interpolation techniques to predict spacecraft trajectories [16, 21–23]. The LCA, as proposed by the authors in [16], is utilized to develop an extrapolation algorithm, the so-called extended LCA (eLCA). The proposed eLCA enables the determination of trajectories beyond the defined interval, facilitating accurate measurements to track objects beyond the interpolation. The LCA produces piece-wise and analytical functions that describe trajectories based on the boundary conditions of intervals within the known spacecraft measurements. Consequently, one can utilize the LCA to obtain the spacecraft's position, velocity, or acceleration at any point within the specified interval, eliminating the need for iterative methods to derive spacecraft trajectories from the outset. To achieve higher computational efficiency, the LCA utilizes a distinct system formulation that allows for the decomposition of the system into lower bi-diagonal matrices and an upper triangular matrix. Through the decomposition of a dense system into sparse matrices, the solving process is completed with fewer operations as compared to brute-force system solving methods. This method of trajectory generation is investigated for interpolation between boundary conditions [16], and demonstrates the ability to sufficiently reproduce trajectories in the CR3BP, at significantly lower computational time compared to conventional iterative methods, given the proper sampling of boundary conditions. The goal of this work is to investigate the extrapolation potential of the algorithm beyond the known boundaries.

Before we proceed with formulating the eLCA, let us recall the LCA. The LCA was formulated based on the spacecraft's position, velocity, and acceleration measurements. Take the position, velocity, and acceleration vectors of the spacecraft are given via, $\underline{r}(t_i)$, $\dot{\underline{r}}(t_i)$, and $\ddot{\underline{r}}(t_i) \in \mathbb{R}^3$, and are known at a time t_i for $i = 0, 1, \cdots, n$ and $t_0 < t_1 < \cdots < t_n$. Knowing $n + 1$ boundary conditions of the spacecraft at distinct times allows for n intervals to be defined based on the boundaries, or over the time interval $I_k = [t_k, t_{k+1}]$, where $k = 0, 1, \cdots, n - 1$. The LCA distinctively executes in each dimension, thus the vector $\underline{r}(t_i) \in \mathbb{R}^3$ is reduced to $x(t_i) \in \mathbb{R}$. Therefore, in a single dimension, the trajectory of the spacecraft over interval I_k is described as

$$G_k(x(t)) = g_{0,k} + g_{1,k}t + g_{2,k}t^2 + g_{3,k}t^3 + g_{4,k}t^4 + g_{5,k}t^5, \tag{4}$$

where $\underline{g}_k = \left[g_{0,k},\ g_{1,k},\ g_{2,k},\ g_{3,k},\ g_{4,k},\ g_{5,k}\right]^T$ represents the coefficients of the polynomials in each interval that depends on the states of the spacecraft at the boundaries of the I_k time interval. The corresponding velocity and acceleration across I_k are then defined using the explicit time derivative:

$$\begin{aligned} \dot{G}_k(x(t)) &= g_{1,k} + 2g_{2,k}t + 3g_{3,k}t^2 + 4g_{4,k}t^3 + 5g_{5,k}t^4, \\ \ddot{G}_k(x(t)) &= 2g_{2,k} + 6g_{3,k}t + 12g_{4,k}t^2 + 20g_{5,k}t^3. \end{aligned} \tag{5}$$

Thus, the coefficient vector ($\underline{g}_k$) shall be determined for each interval to represent the trajectories of the spacecraft in order to determine spacecraft trajectories within the time intervals $I_k = [t_k, t_{k+1}]$ for $k = 0, 1, \cdots, n - 1$. It is important to note that, to ensure a smooth and continuous piece-wise function between time intervals, the boundary conditions connecting two intervals shall be satisfied by the respective polynomials. Thus, utilizing Eqs. (4) - (5) as well as the known position (x), velocity ($\dot{x}$), and acceleration ($\ddot{x}$) of the spacecraft on the boundaries of I_k:

$$\underbrace{\begin{bmatrix} 1 & t_k & t_k^2 & t_k^3 & t_k^4 & t_k^5 \\ 1 & t_{k+1} & t_{k+1}^2 & t_{k+1}^3 & t_{k+1}^4 & t_{k+1}^5 \\ 0 & 1 & 2t_k & 3t_k^2 & 4t_k^3 & 5t_k^4 \\ 0 & 1 & 2t_{k+1} & 3t_{k+1}^2 & 4t_{k+1}^3 & 5t_{k+1}^4 \\ 0 & 0 & 2 & 6t_k & 12t_k^2 & 20t_k^3 \\ 0 & 0 & 2 & 6t_{k+1} & 12t_{k+1}^2 & 20t_{k+1}^3 \end{bmatrix}}_{A_k} \underbrace{\begin{bmatrix} g_{0,k} \\ g_{1,k} \\ g_{2,k} \\ g_{3,k} \\ g_{4,k} \\ g_{5,k} \end{bmatrix}}_{\underline{g}_k} = \underbrace{\begin{bmatrix} x(t_k) \\ x(t_{k+1}) \\ \dot{x}(t_k) \\ \dot{x}(t_{k+1}) \\ \ddot{x}(t_k) \\ \ddot{x}(t_{k+1}) \end{bmatrix}}_{\underline{b}_k}, \tag{6}$$

to determine spacecraft trajectories within the time intervals $I_k = [t_k, t_{k+1}]$ for $k = 0, 1, \cdots, n-1$. From this point, it is possible to take the explicit inverse of A_k within each interval to solve for the polynomial coefficients, $\underline{g}_k$. Note that this approach is computationally expensive, costing $O(n^3)$ operations as one has to determine $6n$ coefficients explicitly. On the other hand, the explicit inverse is rarely computed to solve equations [24]. Thus, to reduce the complexity, the LCA is proposed while factoring A_k into an upper triangular and bi-diagonal matrices such that

$$U_k \underline{g}_k = \tilde{\underline{b}}_k, \quad \text{where} \quad \tilde{\underline{b}}_k = \left(\prod_{r=1}^{5} \tilde{L}_r \right) \underline{b}_k \tag{7}$$

where $U_k \in \mathbb{R}^{6\times6}$ is an upper triangular matrix and $L_r \in \mathbb{R}^{6\times6}$, $r = 1, 2, .., 5$ are bi-diagonal matrices. These matrices and their entries are explicitly shown in the Appendix. Once the bi-diagonal matrices-vector product is computed, $\tilde{\underline{b}}_k$ is obtained. Next, the backward substitution is used with the upper triangular matrices to solve for the coefficient vector $\underline{g}_k$. The computational costs associated with various processes are as follows: the pre-computation of the matrix entries incurs a cost of $O(n)$, while the matrix-vector product involving bi-diagonal matrices to obtain $\tilde{\underline{b}}_k$ also has a complexity of $O(n)$. Moreover, the backward substitution process demands a higher complexity of $O(n^2)$. Thus, the LCA cost $O(n^2)$ as opposed to the brute-force calculation with $O(n^3)$ complexity. For more information on the LCA, refer to [16].

B. The extended LCA (eLCA)

The LCA is determined based on the piecewise and smooth functions derived from position, velocity, and acceleration data, enabling trajectory estimation within the time intervals $I_k = [t_k, t_{k+1}]$ for $k = 0, 1, \cdots, n-1$. Thus, any extrapolation beyond the interval $[t_0, t_n]$ will inevitably deviate from the true dynamics. Hence, the eLCA is proposed to correct this by taking repeated "pseudo-measurements" throughout the extrapolated arc. Based on this point, the position and velocity are derived from the calculation of the LCA-based polynomials. While the acceleration computed using LCA starts to diverge from the original dynamics, it is still possible to estimate an approximate acceleration by utilizing the state from the pseudo-measurement and applying the dynamics of the CR3BP. Despite the inherent error associated with the polynomial approximation in such a state, aligning the acceleration at this juncture with dynamics that more accurately reflect the true behavior helps refine the LCA approximation. This approach effectively mitigates error propagation without necessitating any additional measurements. Hence, the computed acceleration generates a pseudo-measurement state that is utilized alongside the initial measurement point of the arc. By leveraging these two reference points—the first measurement and the newly created pseudo-measurement—a refined LCA trajectory is established, characterized by a reduced rate of error accumulation. This process is then repeated at regular intervals to continually slow down the error propagation significantly. These repeated arc segments are then independently combined to form the predicted arc.

Figure 2 illustrates a diagram based on the eLCA technique. The spacecraft's position, velocity, and acceleration can be measured at two prior points: Measurement 1 (M1) and Measurement 2 (M2). Let these measurements be $\underline{r}(t_{M1}), \dot{\underline{r}}(t_{M1}), \ddot{\underline{r}}(t_{M1})$ for M1, and $\underline{r}(t_{M2}), \dot{\underline{r}}(t_{M2}), \ddot{\underline{r}}(t_{M2})$ for M2. These data are utilized to estimate the spacecraft's trajectories of the form represented in Eq. (4), resulting in the LCA indicated by the dashed black line. This deviates significantly from the true path, represented by the solid black line. At some point along the LCA arc, a pseudo-measurement is taken. In this context, the position and velocity are determined using the LCA, utilizing the Eqs. (4) and (5)-say $\underline{r}(t_{ps}), \dot{\underline{r}}(t_{ps})$, respectively. Meanwhile, the acceleration is derived from the equations of motion referenced in Eq. (1). The measurements $\underline{r}(t_{ps}), \underline{\dot{r}}(t_{ps}), \underline{\ddot{r}}(t_{ps})$, which signify the pseudo-measurement, along with $\underline{r}(t_{M1}), \underline{\dot{r}}(t_{M1}), \underline{\ddot{r}}(t_{M1})$ that correspond to M1, are employed in conjunction with the LCA to obtain the arc depicted in blue. It is important to emphasize that only the segment following the pseudo-measurement is of use. This process is subsequently repeated for each new arc, consistently utilizing M1 as the initial LCA boundary in every calculation. The arcs between pseudo measurements are then combined to form a much better estimate of the trajectory of the spacecraft. The pseudo-code for this process, i.e., eLCA, is shown in Algorithm 1. This process then starts over when given a new true satellite measurement.

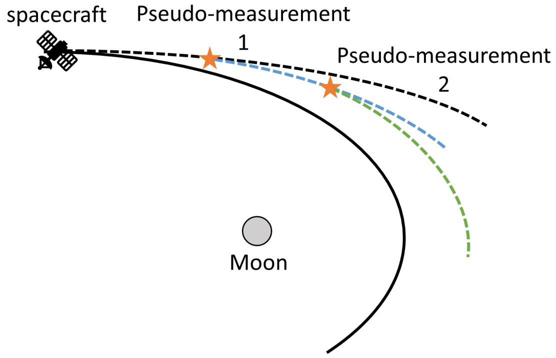

Fig. 2 eLCA diagram with example pseudo-measurements.

Algorithm 1 Pseudo-code for the eLCA

```
Take Measurements M1 and M2
Complete LCA and extrapolate arc
while No New Measurement do
    Make a pseudo-measurement of the previous arc position and velocity at some interval past M2
    Calculate acceleration at pseudo-measurement
    Complete LCA analysis utilizing M1 and pseudo-measurement, forming a new arc
    Append an extrapolated arc segment between the current pseudo-measurement and a new pseudo-measurement to the running eLCA arc
end while
```

One of the benefits of the eLCA is that the spacing of the pseudo-measurements may be varied to balance accuracy requirements with computational costs. Additionally, when calculating a trajectory using the eLCA, the procedure may be immediately discontinued when a new measurement is obtained. However, in the case where satellite measurement frequency is unknown, numerical integration requires the trajectory to be calculated to an arbitrarily far point. This would require excessive and likely unnecessary computation.

IV. Results

To demonstrate the eLCA, simulations are completed using a variety of scenarios. The eLCA is initially tested on the Distant Retrograde Orbit (DRO) [25], as the DRO offers simple, planar dynamics to offer a simple introductory case. Further analysis on the more complex NRHO is conducted. The NRHO provides a dynamically more challenging case, where the trajectory contains dynamically sensitive regions along the perilune of the trajectory. The discrepancy between the slower dynamics near the apoapsis and the rapidly changing dynamics near the periapsis allow for a more nuanced analysis on the performance of the eLCA. Once the details of the eLCA are demonstrated, the eLCA is demonstrated for full orbits across several cases. Throughout this work, all results are presented in the barycentric Earth-Moon rotating frame.

A. Case 1: Distant Retrograde Orbit (DRO)

Initial studies are completed to demonstrate the extent in which the eLCA compounds error in comparison to the LCA when predicting a trajectory in the CR3BP. A simulation of a DRO is completed using both the LCA and eLCA. A

Runge-Kutta integrator of order 5(4) (RK45) is used to propagate the dynamics of the spacecraft and serves as the "truth" model, from which "measurements" for the LCA are obtained, and serves as the benchmark for error comparisons. Generating measurements for the LCA in this manner allows more freedom to the selection of trajectories to be used in the analysis. In real applications, true spacecraft trajectory data may always be inserted. In the simulation, a single orbit consists of 10,000 time steps, divided into eight equal time sections, with the first and last points of each section serving as measurement boundary conditions. The LCA and eLCA then extrapolate past the last boundary condition (final measurement). The interval between consecutive pseudo-measurements for the eLCA is selected to be 20 time-steps, corresponding to approximately 2,300 seconds. The extrapolation was done to 300 time-steps past M2, or approximately 34,300 seconds. The results for a given segment in the DRO are shown in Figure 3. From this demonstration, it is clear that the LCA's poor performance in dynamics prediction results in a quick deviation from the true path. On the other hand, the eLCA is able to predict a trajectory that has a dramatically lower error than the LCA. Particularly, not only is the error lower, but the rate at which the error accumulates is also lower. This means that as time progresses, the eLCA's error reduction gets comparatively better.

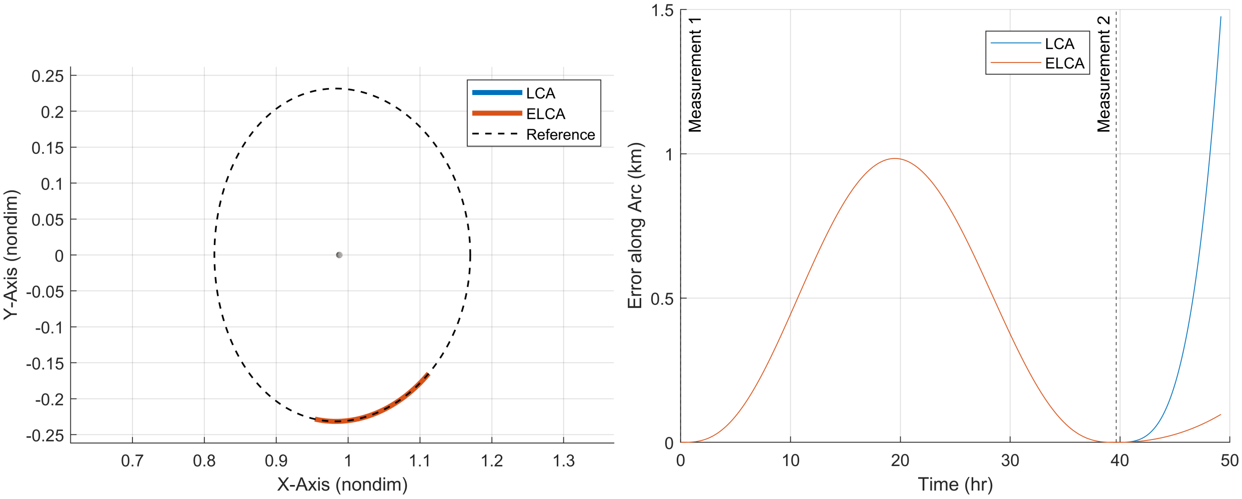

Fig. 3 DRO track (left) and error buildup (right).

One of the most influential variables associated with the eLCA is the pseudo-measurement interval. As noted in section III, the pseudo-measurements are regularly taken from the resulting trajectory arc that corresponds to M1 and the previous pseudo-measurement. The interval between pseudo-measurements directly influences the frequency with which the CR3BP dynamics are reintroduced into the trajectory estimate, correlating to the extent to the error buildup rate. A study is completed to compare various pseudo-measurement intervals for the DRO (Figure 4). For context, the simulations are completed with each orbit consisting of 10,000 time-steps. This results in each time-step being approximately 114.3 seconds. The extrapolation was then completed to 600 time-steps past M2. These results demonstrate that even with a relatively coarse time step of up to 50 time-steps, the eLCA still provides a drastic improvement compared to the LCA. When looking at interval lengths of 10 to 50-time steps, there appears to be a nearly linear spacing between errors, indicating that the relationship between error buildup rate and interval length is nearly linear. However, it is crucial to note the primary reason pseudo-measurements are not taken at an unreasonably high rate is due to the increased computation time required. To demonstrate this trade-off with computation time and interval length, the above eLCA analysis with varying pseudo-measurement intervals is completed and timed. The computation time is averaged over 1000 runs to minimize random errors in hardware computation. The results are summarized in Figure 5 comparing the final error of the arc shown in Figure 4 with the computation time. It should be noted that the measured computation time includes both calculating the LCA coefficients as well as completing the extrapolation to find the states at each position in time.

From these results, it is seen that decreasing the interval between pseudo-measurements increases the computation time to varying extents. At every new pseudo-measurement, the eLCA executes a run of the LCA, which operates at a fixed arithmetic. The fixed arithmetic defines a linear relationship between number of pseudo-measurements (i.e., number of times the LCA runs) and total computation time. However, there seems to be diminishing returns in computational efficiency with the eLCA. For example, the computation time using pseudo-measurement intervals of 20

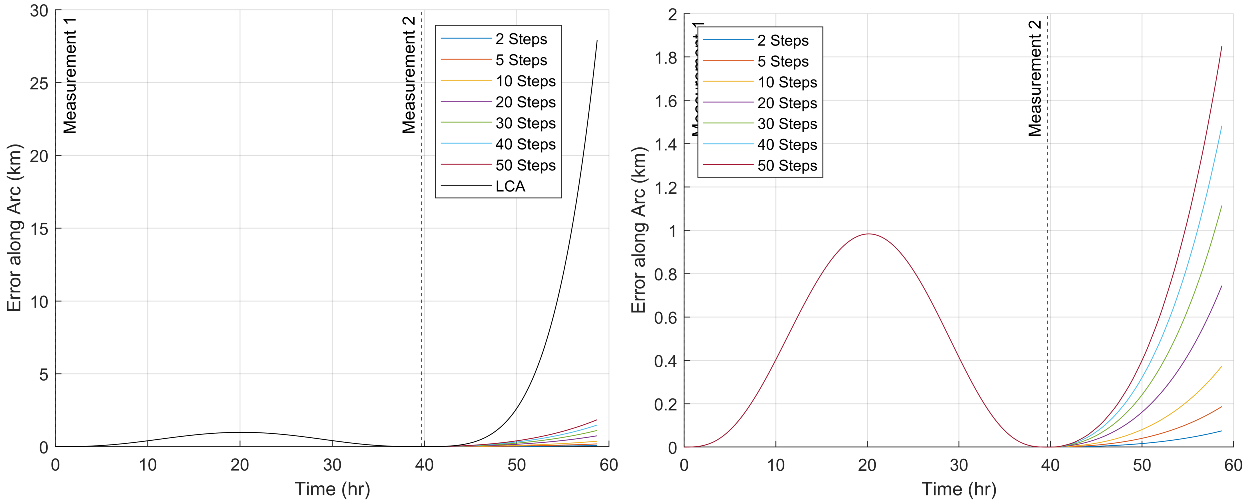

Fig. 4 **eLCA error comparison for various pseudo-measurement intervals in the DRO, zoomed on right.**

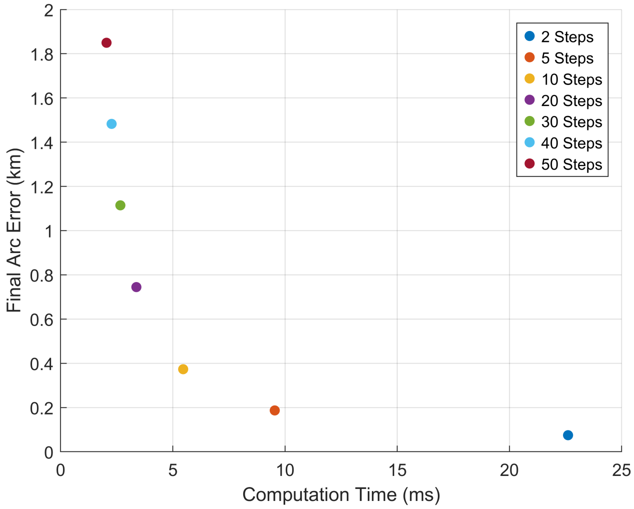

Fig. 5 **eLCA error and computation time for various pseudo-measurement intervals in the DRO (System: Intel i5-9300H, 8.0 GB memory).**

time-steps is a noticeably larger than half of the computation time of an eLCA with pseudo-measurement intervals of 10 time-steps. This benefit continually decreases approaching larger interval lengths. Despite this, as noted previously, the final error in the arc appears to be nearly linear with the various interval lengths. This means that for a given mission, error requirements, and computational limits, there is likely some optimal interval length.

B. Case 2: Near-rectilinear Halo Orbit (NRHO)

To demonstrate a more challenging case to the eLCA, the analysis is now conducted on an NRHO. Similar to the DRO, the NRHO orbit is divided into eight equal segments over 10,000 time steps, with the endpoints of each segment used as measurement boundary conditions. The LCA and eLCA are then used to extrapolate past the measurement points. For the eLCA, pseudo-measurements are spaced at 20 time-steps (approximately 1,149.6 seconds), with extrapolations extending 300 time-steps past M2 (around 17,245 seconds). Due to the drastic difference in dynamics between the apoapsis and periapsis of the orbit, two segments along each section are analyzed. The results for a segment near the apoapsis of the orbit are shown in Figure 6, and a segment near the periapsis is shown in Figure 7.

Similar to the results of the DRO, these results illustrate that the eLCA significantly reduces the error build-up

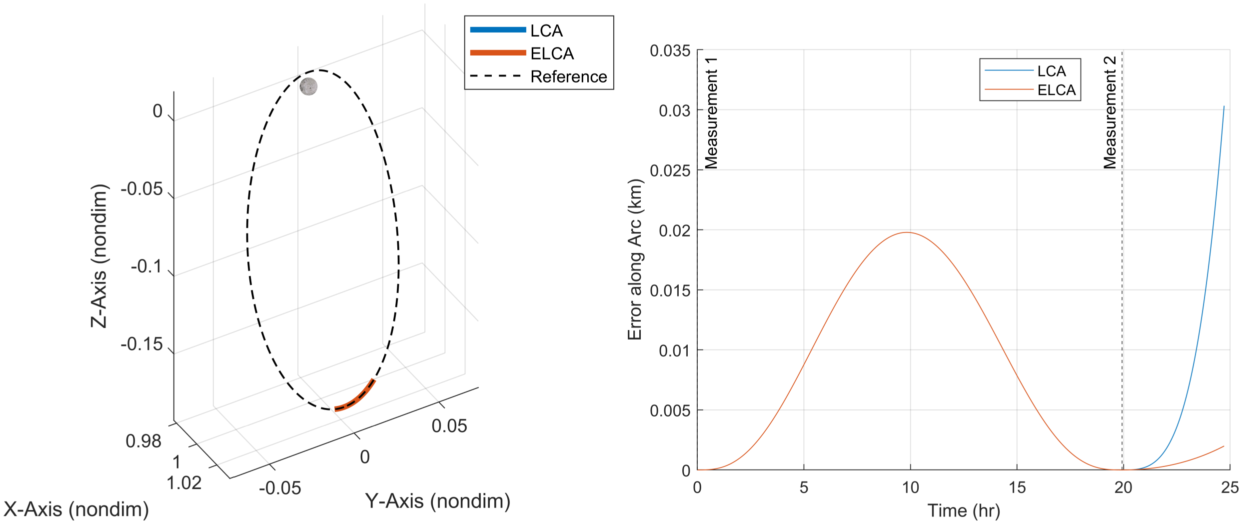

Fig. 6 NRHO apoapsis track (left) and error buildup (right).

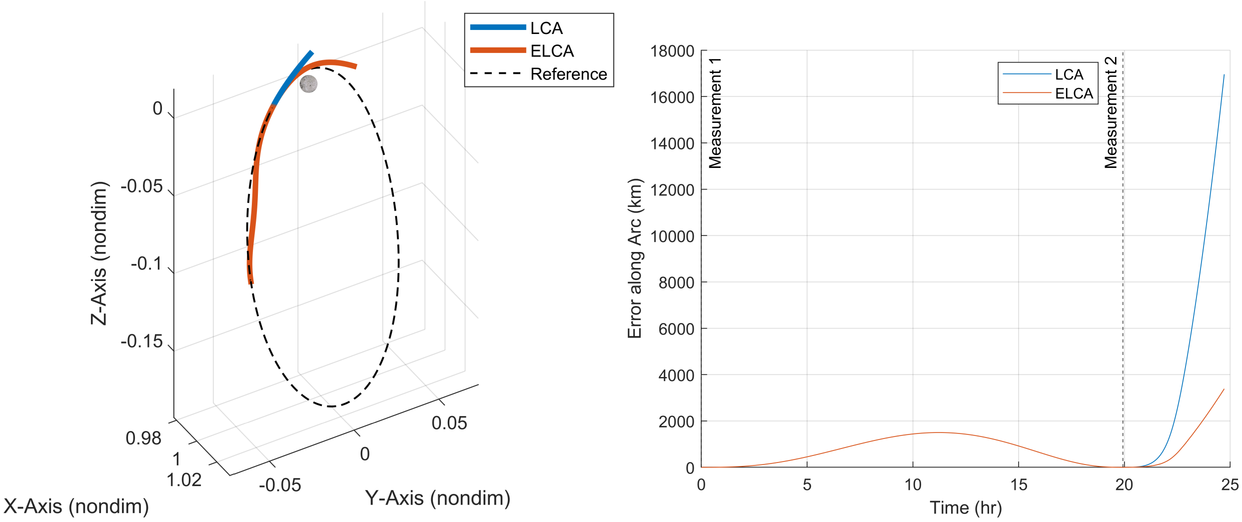

Fig. 7 NRHO periapsis track (left) and error buildup (right).

compared to the LCA. A closer inspection of the results, particularly near periapsis, shows the extent to which the dynamics start to quickly deviate. When looking at the track on the left side of Figure 7, it is immediately seen that the LCA track deviates further laterally from the true orbit. On top of this, it is seen that the distance of the LCA extrapolation is much shorter than the eLCA extrapolation. Approaching the periapsis of an eccentric orbit, the spacecraft is expected to speed up due to the increasing gravitational force. However, the short distance traveled in the LCA arc indicates that the LCA fails to account for these dynamics and does not speed up the estimated trajectory of the orbiting object. Although directly comparing the results from the apoapsis and periapsis demonstrations may appear to show that the eLCA provides more error reduction for portions of an orbit with slower dynamics, like the apoapsis of the NRHO, this is not the case. As will be shown in further analysis, there are a very large number of factors that influence the error build up rate for the eLCA.

To determine what selection of measurement points may be optimal for an eLCA estimation, an analysis is completed using boundary points further away from the pseudo-measurements to find a potentially optimal spacing between measurement points for the eLCA extrapolation. For the NRHO, similar to the initial simulation discussed, the full orbit is divided into 8 segments of equal time. The LCA and eLCA extrapolations are completed for "Far" and "Close" measurement, consisting of M1 to M2 distances of $\frac{1}{4}$th of an orbit and $\frac{1}{8}$th of an orbit, respectively. This analysis is done for both insensitive and sensitive portions of the NRHO, as seen in Figures 8 and 9, respectively. In Figure 8, it is seen that with the relatively tame dynamics near the apoapsis of the NRHO, a closer distance between M1 and M2 provides significantly better results for the extrapolation of both the LCA and the eLCA. Figure 9 suggests that the opposite is true in situations with stronger dynamics. When the trajectory arc is set to extrapolate the spacecraft's path just after the periapsis of the NRHO, there is a slight decrease in error for both the LCA and eLCA with a further distance between M1 and M2. This suggests that for a given M2 after which an LCA or eLCA analysis is completed, there is some optimal M1 point that leads to the smallest error build up rate in the predicted trajectory. This optimal point is a function of the dynamics in the region of interest. Due to the polynomial nature of the LCA and eLCA, utilizing information about the jerk along the trajectory may provide an opportunity to further decrease error without numerical integration.

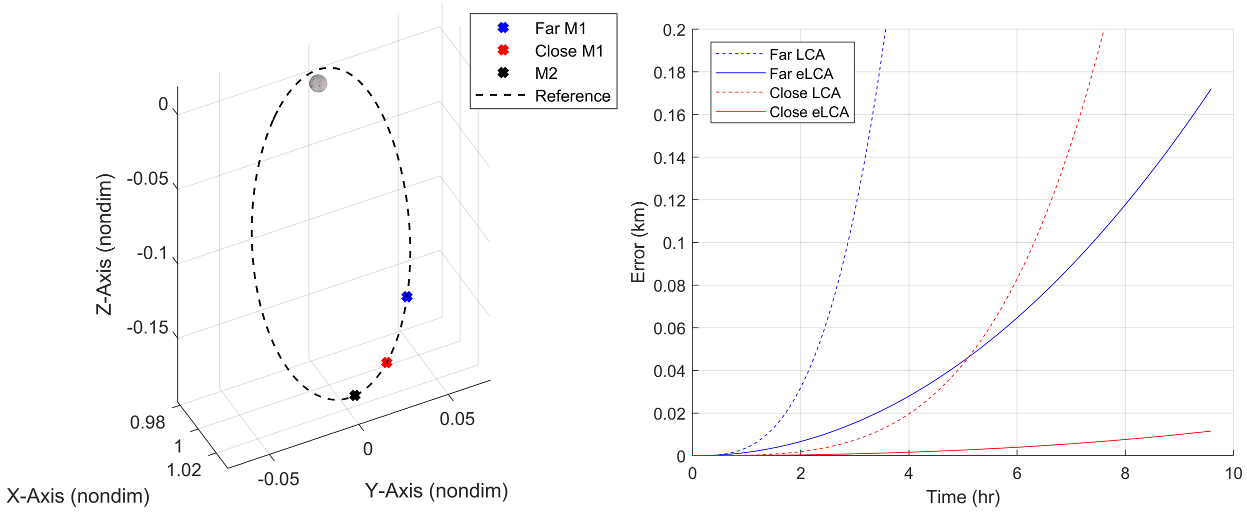

Fig. 8 NRHO low dynamics M1 points track (left) and error buildup (right).

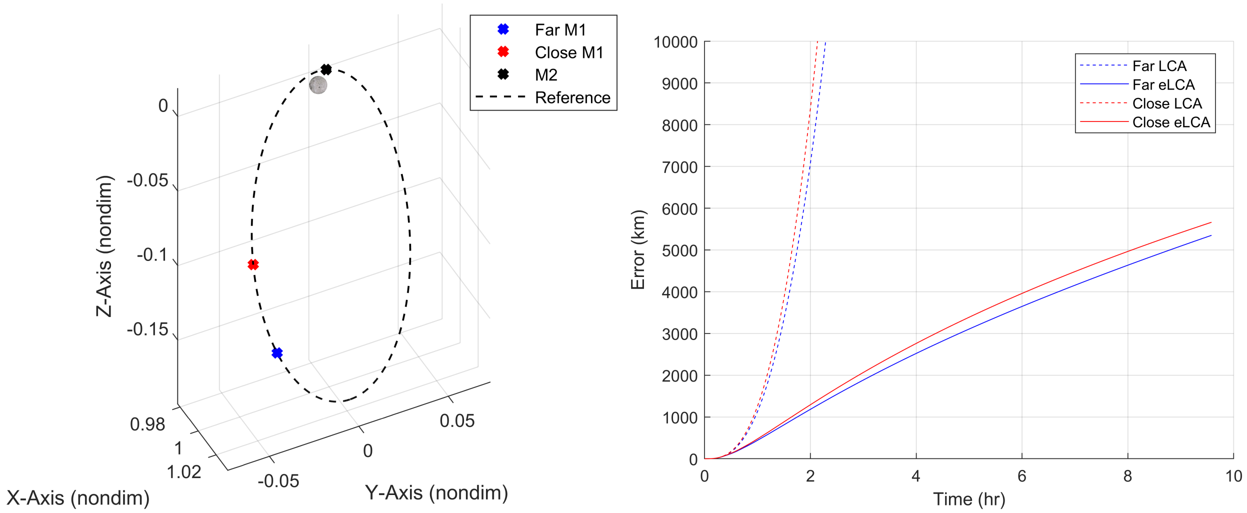

Fig. 9 NRHO high dynamics M1 points track (left) and error buildup (right).

In addition to establishing the optimal boundary points for the LCA and eLCA, another important factor affecting error buildup in the eLCA is the interval between pseudo-measurements. As described in Section III, these measurements are taken along the arc between M1 and the prior pseudo-measurement. The measurement's spacing significantly influences the propagation of errors in the polynomial model. Similar to the DRO case, a study is conducted to compare different pseudo-measurement intervals. Specifically, near the periapsis of the NRHO where the fastest rate of error buildup is previously seen. The subsequent results are shown in Figure 10. For context, the simulations are completed with each orbit consisting of 10,000 time-steps. This results in each time-step being approximately 57.3 seconds. The extrapolation is then completed to 600 time-steps past M2. As shown, even relatively coarse intervals of up to 50 time-steps result in a marked improvement with the eLCA compared to the LCA. The nearly linear increase in error between intervals of 10 to 50 time-steps mirrors the trend seen in the DRO case, indicating a proportional relationship between interval length and error accumulation. However, as before, the key trade-off is the increased computational cost associated with shorter intervals.

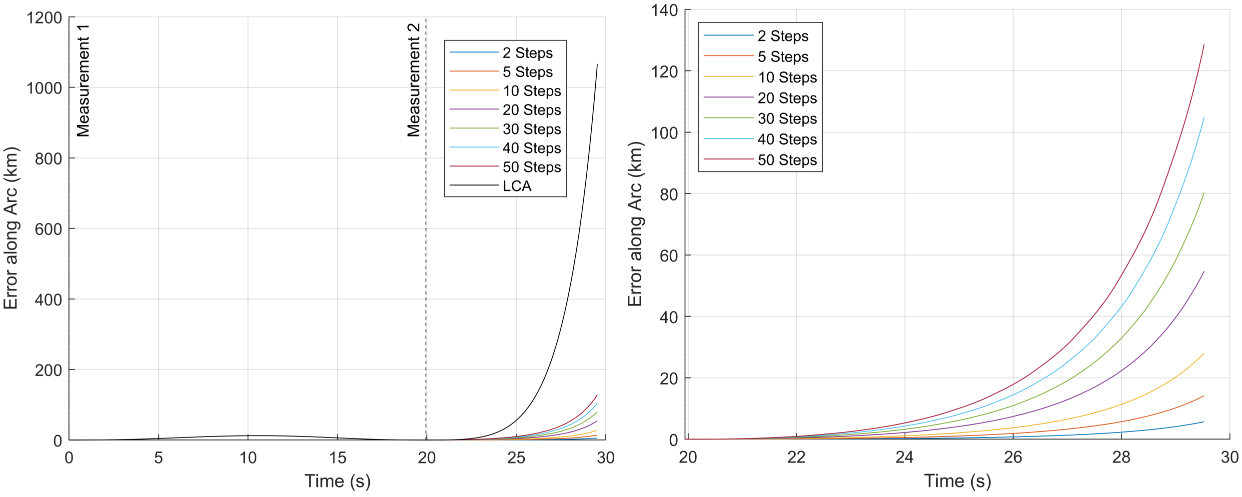

Fig. 10 eLCA error comparison for various pseudo-measurement intervals in the NRHO, zoomed on right.

To evaluate computation times for different interval lengths, the eLCA is executed and the times are averaged over 1,000 runs to reduce random errors, following a similar approach to the DRO analysis. The results are summarized in Figure 11 comparing the final error of the arc shown in Figure 10 with the computation time. As with the DRO case, it should be noted that the measured computation time includes both calculating the LCA coefficients as well as completing the extrapolation to find the states at each position in time. Similar to the DRO case, reducing the interval between pseudo-measurements leads to a nearly linear increase in computation time. Each new pseudo-measurement requires a complete LCA analysis, establishing a direct relationship between the number of measurements and total computation time. However, diminishing returns become evident; for instance, the computation time for 20 time-steps is noticeably more than half of that required for 10 time-steps. This diminishing efficiency highlights the need to balance error reduction and computational resources based on mission-specific requirements, error tolerances, and available processing power.

C. Full Orbit Demonstrations

The results presented thus far characterized the performance of the eLCA in small test cases. However, the eLCA shall be compared to LCA over the course of a full orbit. For high SDA, orbits may have to be tracked with a limited number of measurements. As a result, a simulation is devised, providing a comprehensive investigation of tracking over a full orbit. In this simulation, a short, initial section of the orbit is used to initialize the first arc, with the first and last points of this arc serving as the M1 and M2 for the subsequent LCA or eLCA extrapolation. While propagating, the error is continuously monitored. Once the error exceeds some arbitrarily set error threshold, the extrapolation is stopped, and a point from the numerically integrated arc is used as a new measurement. The previous M2 serves as the new M1, and the new measurement serves as M2. Using these two boundary points, a new extrapolation is completed. Over a full orbit, the total number of measurements needed to keep the error below the set threshold is compared for the LCA and eLCA. This is then completed with a range of orbits to characterize the performance of LCA and eLCA extrapolation for a range of Cislunar dynamics. In each simulation, a full orbit consists of 10,000 time-steps, with the true time of each time-step varying by orbit. The first 100 time-steps are used for the initialization, and for the eLCA extrapolation, a pseudo-measurement interval of 20 time-steps is selected as a reasonable balance between error and

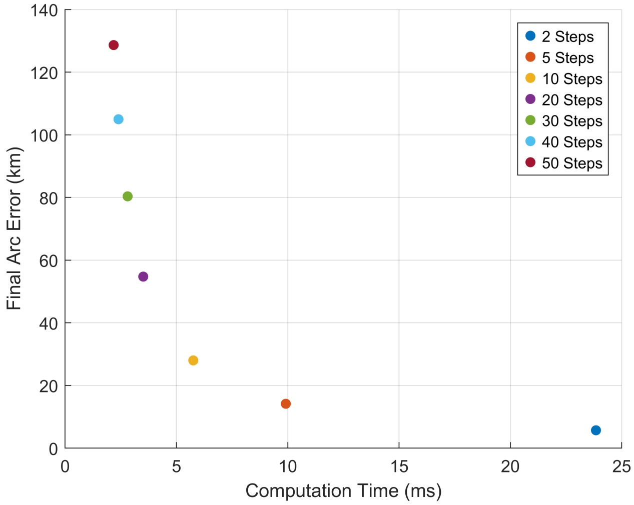

Fig. 11 eLCA error and computation time for various pseudo-measurement intervals in the NRHO (System: Intel i5-9300H, 8.0 GB memory).

computation, as seen in Figure 11.

The first demonstrated orbit is the NRHO, due to the highly varying dynamics across the orbit. The full orbit takes 572,640 seconds, or about 6.63 days. For comparison, two runs are completed, one utilizing 25 km as the error threshold, and another utilizing 100 km, with the results shown in Figures 12 and 13, respectively. As expected, to maintain a lower error threshold, more measurements are needed to adjust for the varying dynamics, through comparisons between the corresponding sides of Figures 12 and 13. In addition, the distribution of the eLCA measurements sheds light on the manner in which the eLCA may be optimized. As the object approaches the apoapsis, the eLCA requires regular, but increasingly spaced measurements to maintain a low error. Immediately before reaching apoapsis, there is a relatively quick change in orbital radius, as is typical on the periapsis and apoapsis of an elliptical orbit. After this measurement just prior to the apoapsis, the tracked object remains well track for a long portion of the flight. In further studies to optimize the use of the eLCA, this may provide insight for choosing optimally spaced boundary points. Finally, through these simulations, it is clear that in both cases, the eLCA dramatically reduces the total number of needed measurements to keep the error below the threshold. In the case of a 25 km error limit, the LCA and eLCA required 26 and 15 measurements, respectively, including the two measurements used for initialization. In the case of a 100 km error limit, the LCA and eLCA required 21 and 11 measurements, respectively, including the two measurements used for initialization. From the analysis of the test case shown in Figure 10, it was seen that at all points, the rate of change of the slope was always higher for the LCA than the eLCA. This means that not only is the error rate always higher for the LCA, but this error rate also grows faster for the LCA compared to the eLCA, proving that the LCA's predictions tend to have errors that compound to deviate from the true dynamics as time progresses. As a result, when the LCA and eLCA are used for trajectory extrapolation, the performance benefits of the eLCA relative to the LCA improve with extrapolation distance. This is directly seen in the demonstrated results as the eLCA orbit required $\sim 42\%$ fewer measurements than the LCA with a 25 km error threshold while the eLCA required $\sim 48\%$ fewer measurements than the LCA with a 100 km error threshold.

This analysis is next completed for a DRO and a Lyapunov orbit around the L_2 point in the Earth-Moon system to study the eLCA over key Cislunar trajectories. These results are shown in Figures 14 and 15 for the DRO and L_2 Lyapunov orbits, respectively. For each test, an error threshold was chosen that would allow for a proper comparison between the LCA and eLCA. With an error threshold too small for a given orbit, there would not be enough pseudo-measurements taken to properly show the benefits of the eLCA. With an error threshold too large, the eLCA may not take enough measurements to demonstrate the limitations of the eLCA. In the DRO simulation, an error threshold of 50 km is selected, resulting in the LCA and eLCA requiring 15 measurements and 6 measurements, respectively, including the two measurements used to initialize the trajectory. In the L_2 Lyapunov simulation, an error threshold of 25 km is selected, resulting in the LCA and eLCA requiring 11 and 4 measurements, respectively, including the two measurements used to initialize the trajectory. The total results are summarized in Table 1. As demonstrated, the eLCA provides significant improvements compared to the LCA in trajectory prediction, minimizing the need for large numbers of measurements to

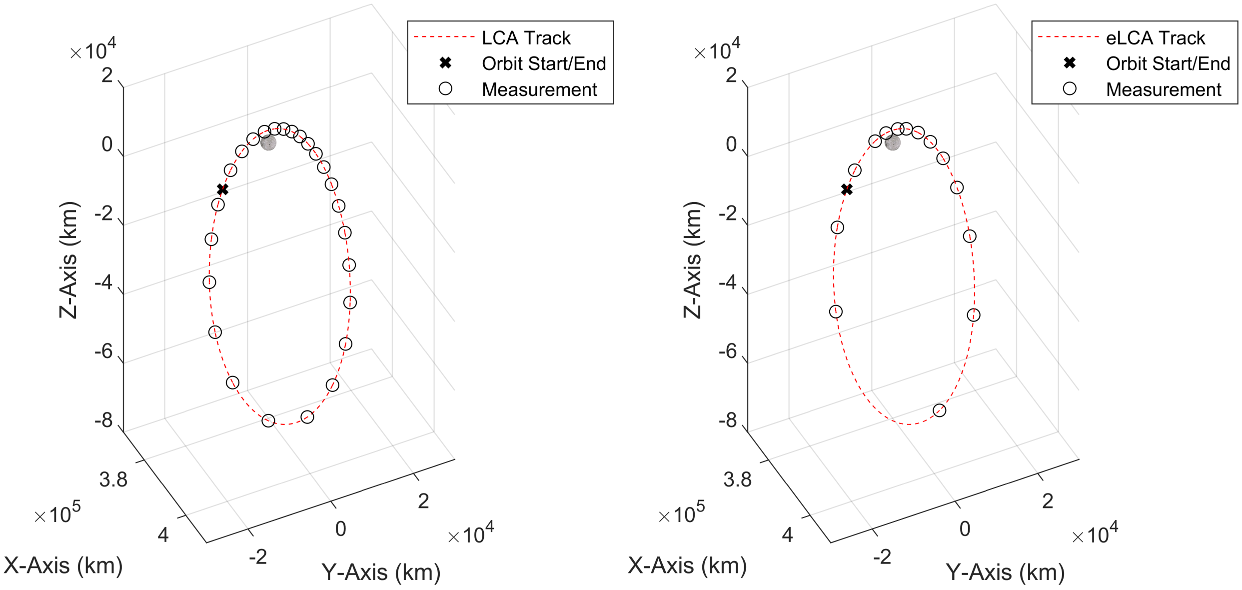

Fig. 12 NRHO full orbit tracking with LCA (left) and eLCA (right) with an error threshold of 25 km.

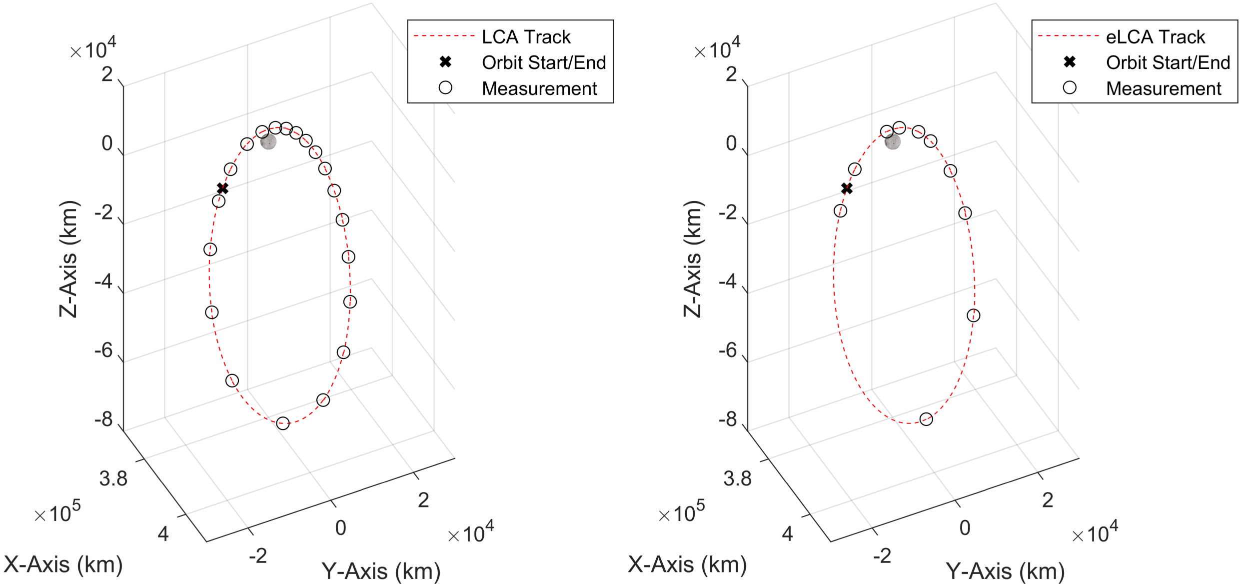

Fig. 13 NRHO full orbit tracking with LCA (left) and eLCA (right) with an error threshold of 100 km.

extrapolate the trajectory of a body in complex dynamics.

Table 1 Full orbit extrapolation summary.

Orbit	LCA Measurements	eLCA Measurements	Required Measurements Decrease
NRHO, 25 km error	26	15	42.31%
NRHO, 100 km error	21	11	47.62%
DRO, 50 km error	15	6	60.00%
L_2 Lyap, 25 km error	11	4	63.64%

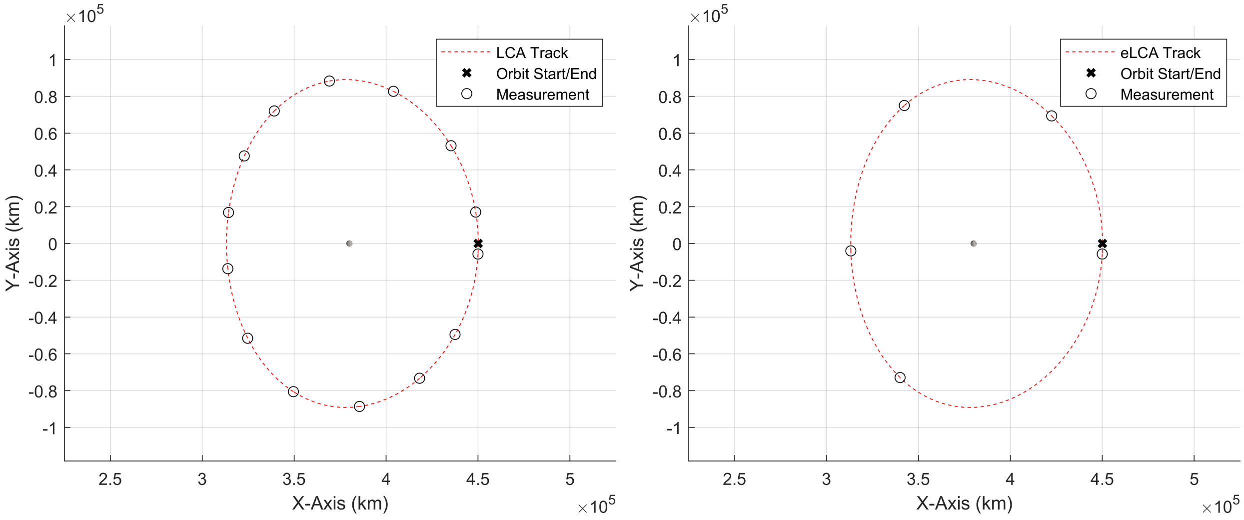

Fig. 14 DRO full orbit tracking with LCA (left) and eLCA (right), error threshold of 50 km.

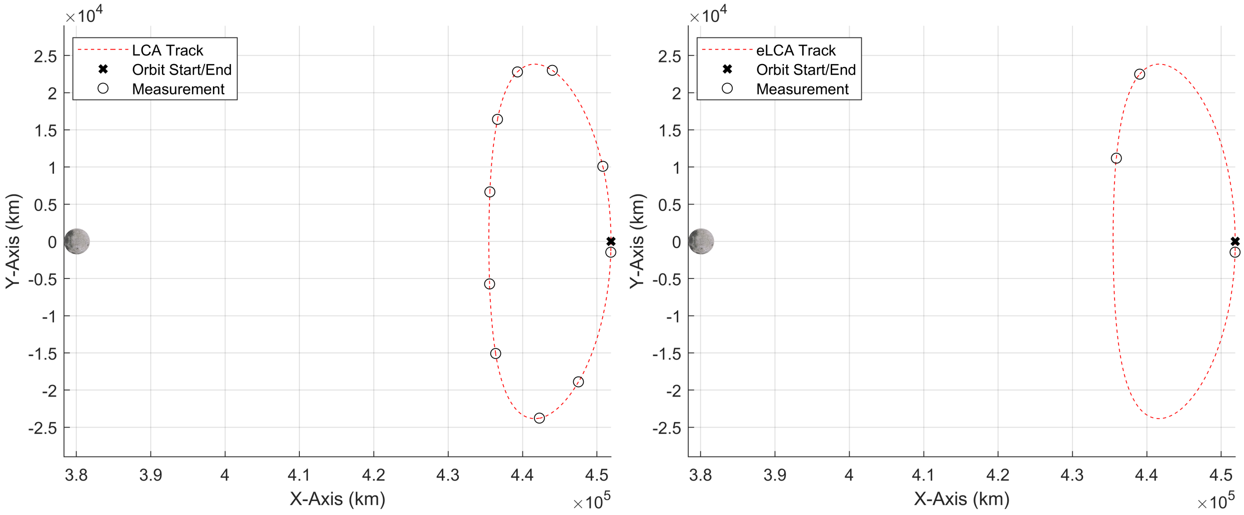

Fig. 15 L_2 Lyapunov full orbit tracking with LCA (left) and eLCA (right), error threshold of 25 km.

V. Conclusion

In this work, the eLCA is introduced, building on the previously developed LCA. The eLCA incorporates knowledge of the system's dynamics into the LCA measurements to allow for high accuracy in orbit trajectory prediction. As demonstrated, the eLCA significantly improves performance relative to the LCA in the CR3BP. In certain SDA problems, such as tracking objects in different orbits, or tracking large amounts of objects at once, the number of measurements made should be minimized. The eLCA demonstrates its ability to accurately track objects while minimizing position estimate errors. The eLCA is proven to require minimal measurements for orbits with low and consistent dynamics throughout the full period, such as the DRO and L_2 Lyapunov orbits. Due to the highly varying dynamics in the NRHO, the eLCA comparatively requires more measurements compared to the other demonstrated orbits. Regardless, the eLCA is still proven to improve tracking estimates compared to the LCA. Additionally, insight has been gained into opportunities to optimize the measurement locations for the eLCA. For any location in an orbit, there exist some optimal boundary points to minimize the eLCA's error depending on the local dynamics. Finally, the performance benefits and losses associated with varied eLCA pseudo-measurement spacing are analyzed. The eLCA can be further developed by analyzing methods to determine the most optimal measurement points for a given orbit, potentially allowing for additional performance gains by requiring fewer measurements and decreasing error when tracking an object. There also exist many opportunities to refine the eLCA to decrease error as well as computation time, such as utilizing varying pseudo-measurement intervals to optimize the algorithm for the local dynamics.

VI. Acknowledgment

Assistance from colleagues in the Space Trajectories and Applications Research group at Embry-Riddle Aeronautical University is acknowledged as is the support from the Aerospace Engineering department. This work was partially funded by the National Science Foundation Science with the award number 2410676.

Appendix

Consider the one-dimensional position, velocity, and acceleration of a spacecraft, $x(t), \dot{x}(t), \ddot{x}(t) \in \mathbb{R}$, at known times t_k and t_{k+1} on the boundaries of the I_k where $k = 0, 1, \cdots, n-1$. Note that there are $n+1$ known spacecraft states at distinct times. The resulting bi-diagonal and upper triangular matrices from the decomposition of Eq. (6) are found to be:

$$
\tilde{L}_1 = \begin{bmatrix} 1 & & & & & \\ -\tilde{d}_k & \tilde{d}_k & & & & \\ & & 1 & & & \\ & & -\tilde{d}_k & \tilde{d}_k & & \\ & & & & 1 & \\ & & & & -\tilde{d}_k & \tilde{d}_k \end{bmatrix}, \quad \tilde{L}_2 = \begin{bmatrix} 1 & & & & & \\ & 1 & & & & \\ & \tilde{d}_k & -\tilde{d}_k & & & \\ & & & 1 & & \\ & & & \tilde{d}_k & -\tilde{d}_k & \\ & & & & & 1 \end{bmatrix},
$$

$$
\tilde{L}_3 = \begin{bmatrix} 1 & & & & & \\ & 1 & & & & \\ & & 1 & & & \\ & & -2\tilde{d}_k & \tilde{d}_k & & \\ & & & & 1 & \\ & & & & -2\tilde{d}_k & \tilde{d}_k \end{bmatrix}, \quad \tilde{L}_4 = \begin{bmatrix} 1 & & & & & \\ & 1 & & & & \\ & & 1 & & & \\ & & & 1 & & \\ & & & 3\tilde{d}_k & -\tilde{d}_k & \\ & & & & & 1 \end{bmatrix},
$$

$$
\tilde{L}_5 = \begin{bmatrix} 1 & & & & & \\ & 1 & & & & \\ & & 1 & & & \\ & & & 1 & & \\ & & & & 1 & \\ & & & & -2\tilde{d}_k & \tilde{d}_k \end{bmatrix}, \quad U_k = \begin{bmatrix} 1 & t_0 & t_0^2 & t_0^3 & t_0^4 & t_0^5 \\ & 1 & c_{1,k} & c_{2,k} & c_{3,k} & c_{4,k} \\ & & 1 & e_{1,k} & e_{2,k} & e_{3,k} \\ & & & 1 & 2c_{1,k} & f_k \\ & & & & 2 & 2m_k \\ & & & & & 2 \end{bmatrix} \tag{8}
$$

in which the pre-computed entries are given by

$$
\begin{aligned}
\tilde{d}_k &= \frac{1}{t_{k+1} - t_k}, \\
c_{1,k} &= t_{k+1} + t_k, \\
c_{2,k} &= (t_{k+1})^2 + t_{k+1} t_k + (t_k)^2, \\
c_{3,k} &= (t_{k+1})^3 + (t_{k+1})^2 t_k + t_{k+1} (t_k)^2 + (t_k)^3, \\
c_{4,k} &= (t_{k+1})^4 + (t_{k+1})^3 t_k + (t_{k+1})^2 (t_k)^2 + t_{k+1} (t_k)^3 + (t_k)^4, \\
e_{1,k} &= t_{k+1} + 2t_k, \\
e_{2,k} &= (t_{k+1})^2 + 2t_{k+1} t_k + 3(t_k)^2, \\
e_{3,k} &= (t_{k+1})^3 + 2(t_{k+1})^2 t_k + 3t_{k+1} (t_k)^2 + 4(t_k)^3, \\
f_k &= 3(t_{k+1})^2 + 4t_{k+1} t_k + 3(t_k)^2, \\
m_k &= 2t_{k+1} + 3t_k
\end{aligned} \tag{9}
$$

where the lower bi-diagonal triangular matrix $\tilde{L}_r \in \mathbb{R}^{6\times 6}$, $r = 1, 2, .., 5$, upper triangular matrix $U_k \in \mathbb{R}^{6\times 6}$, and the empty entries in the matrices represent zeros. These matricies and quantities are then used to formulate the LCA system shown in Eq. (7).

References

[1] Baker-McEvilly, B., Doroba, S., Gilliam, A., Criscola, F., Canales, D., Frueh, C., and Henderson, T., "A review on hot-spot areas within the Cislunar region and upon the Moon surface, and methods to gather passive information from these regions," *AAS/AIAA 33rd Space Flight Mechanics Meeting*, 2023.

[2] "Artemis Plan; NASA's Lunar Exploration Program Overview," NASA, 2020.

[3] Kazmerchuk, P. V., and Shirshakov, A. E., "The Luna-25 Spacecraft: Return to the Moon," *Solar System Research*, Vol. 55, No. 6, 2021, pp. 496–508. https://doi.org/10.1134/S0038094621060058.

[4] Li, C., Wang, C., Wei, Y., and Lin, Y., "China's present and future lunar exploration program," *Science*, Vol. 365, No. 6450, 2019, pp. 238–239. https://doi.org/10.1126/science.aax9908.

[5] Williams, J., Lee, D. E., Whitley, R. J., Bokelmann, K. A., Davis, D. C., and Berry, C. F., "Targeting Cislunar Near Rectilinear Halo Orbits for Human Space Exploration," AAS/AIAA Space Flight Mechanics Meeting, 2017.

[6] Lee, D. E., "White Paper: Gateway Destination Orbit Model: a Continuous 15 year NRHO Reference Trajectory," Tech. rep., 2019.

[7] Williamson, M., "Lunar exploration and development—A sustainable model," *Acta Astronautica*, Vol. 57, No. 2, 2005, pp. 161–166. https://doi.org/https://doi.org/10.1016/j.actaastro.2005.02.002, infinite Possibilities Global Realities, Selected Proceedings of the 55th International Astronautical Federation Congress, Vancouver, Canada, 4-8 October 2004.

[8] Boone, N., and Bettinger, R., "Simulation of Debris Events in Selected Low Lunar Orbits," *The Journal of the Astronautical Sciences*, Vol. 70, No. 3, 2023. https://doi.org/10.1007/s40295-023-00382-y.

[9] Boone, N., and Bettinger, R., "Monte Carlo simulation of spacecraft breakup events in Low Lunar Orbit," *Advances in Space Research*, Vol. 73, No. 12, 2024, pp. 6125–6139. https://doi.org/https://doi.org/10.1016/j.asr.2024.03.005.

[10] Holzinger, M. J., Chow, C. C., and Garretson, P., "A Primer on Cislunar Space," Air Force Research Laboratory, 2021.

[11] Badura, G., Shimane, Y., Gregoire, A., Patel, R., Gilmartin, M., Gangolli, K., Visonneau, L., Tysor, J., Manojkumar, S., Humphrey, F., et al., "System design and analysis for cislunar space domain awareness through distributed sensors," *AAS/AIAA Astrodynamics Specialist Conference, Charlotte, NC*, 2022, pp. 1–20.

[12] Frueh, C., Howell, K., DeMars, K. J., and Bhadauria, S., "Cislunar space situational awareness," *31st AIAA/AAS Space Flight Mechanics Meeting*, 2021, pp. 6–7.

[13] Aristoff, J. M., Horwood, J. T., and Poore, A. B., "Orbit and uncertainty propagation: a comparison of Gauss-Legendre-, Dormand-Prince-, and Chebyshev-Picard-based approaches," *Celestial Mechanics and Dynamical Astronomy*, Vol. 118, No. 1, 2014, pp. 13–28. https://doi.org/10.1007/s10569-013-9522-7.

[14] Deuflhard, P., "Order and Stepsize Control in Extrapolation Methods," *Numerische Mathematik*, Vol. 41, 1983, pp. 399–422.

[15] Peinado, J., Ibáñez, J., Arias, E., and Hernández, V., "Adams–Bashforth and Adams–Moulton methods for solving differential Riccati equations," *Computers Mathematics with Applications*, Vol. 60, No. 11, 2010, pp. 3032–3045. https://doi.org/https://doi.org/10.1016/j.camwa.2010.10.002.

[16] Canales, D., M. Perera, S., Kurttisi, A., and Baker-McEvilly, B., "A Low-Complexity Algorithm to Determine Trajectories Within the Circular Restricted Three-Body Problem," *Journal of the Astronautical Sciences*, Vol. 70, No. 46, 2023. https://doi.org/https://doi.org/10.1007/s40295-023-00416-5.

[17] Baker-McEvilly, B., Bhadauria, S., Canales, D., and Frueh, C., "A comprehensive review on Cislunar expansion and space domain awareness," *Progress in Aerospace Sciences*, Vol. 147, 2024. https://doi.org/https://doi.org/10.1016/j.paerosci.2024.101019, URL https://www.sciencedirect.com/science/article/pii/S0376042124000459.

[18] Poincaré, H., *Les méthodes nouvelles de la mécanique céleste*, Gauthier-Villars et Fils, Paris, France, 1892. https://doi.org/10.1007/BF02742713.

[19] Szebehely, V., *The General and Restricted Problems of Three Bodies*, Springer, Vienna, 1974. https://doi.org/10.1007/978-3-7091-2916-6.

[20] Aristoff, J. M., Horwood, J. T., and Poore, A. B., "Orbit and uncertainty propagation: a comparison of Gauss-Legendre-, Dormand-Prince-, and Chebyshev-Picard-based approaches," *Celestial Mechanics and Dynamical Astronomy*, Vol. 118, No. 1, 2014, pp. 13–28. https://doi.org/10.1007/s10569-013-9522-7.

[21] Horemuz, M., and Andersson, J., “Polynomial interpolation of GPS satellite coordinates,” *GPS Solutions*, Vol. 10, 2021, pp. 67–72. https://doi.org/https://doi.org/10.1007/s10291-005-0018-0.

[22] Karepova, E., and Petrakova, V., “The comparison of several approaches to the interpolation of a trajectory of a navigation satellite,” *IOP Conference Series: Materials Science and Engineering*, Vol. 537, 2019. https://doi.org/10.1088/1757-899X/537/2/022054.

[23] Geul, J., Mooij, E., and Noomen, R., “Regularised Methods for High-Efficiency Propagation,” *AAS Astrodynamics Specialist Conference*, 2015.

[24] Higham, N. J., *Accuracy and Stability of Numerical Algorithms*, SIAM, Philadelphia, USA, 1996.

[25] Ming, X., and Shijie, X., “Exploration of distant retrograde orbits around Moon,” *Acta Astronautica*, Vol. 65, No. 5, 2009, pp. 853–860. https://doi.org/https://doi.org/10.1016/j.actaastro.2009.03.026, URL https://www.sciencedirect.com/science/article/pii/S0094576509001404.